J. Fluid Mech. (2012), *vol.* 712, *pp.* 41–60.
doi:10.1017/jfm.2012.393

Shape effects on turbulent modulation by large nearly neutrally buoyant particles

Gabriele Bellani[1,2]†, Margaret L. Byron[1], Audric G. Collignon[1], Colin R. Meyer[1] and Evan A. Variano[1]

[1] Department of Civil and Environmental Engineering, University of California, Berkeley, CA 94720, USA

[2] Linné Flow Centre, KTH Mechanics, SE-100 44 Stockholm, Sweden

(Received 1 February 2012; revised 31 July 2012; accepted 1 August 2012; first published online 27 September 2012)

We investigate dilute suspensions of Taylor-microscale-sized particles in homogeneous isotropic turbulence. In particular, we focus on the effect of particle shape on particle–fluid interaction. We conduct laboratory experiments using a novel experimental technique to simultaneously measure the kinematics of fluid and particle phases. This uses transparent particles having the same refractive index as water, whose motion we track via embedded optical tracers. We compare the turbulent statistics of a single-phase flow to the turbulent statistics of the fluid phase in a particle–laden suspension. Two suspensions are compared, one in which the particles are spheres and the other in which they are prolate ellipsoids with aspect ratio 2. We find that spherical particles at volume fraction $\phi_v = 0.14\,\%$ reduce the turbulent kinetic energy (TKE) by 15 % relative to the single-phase flow. At the same volume fraction (and slightly smaller total surface area), ellipsoidal particles have a much smaller effect: they reduce the TKE by 3 % relative to the single-phase flow. Spectral analysis shows the details of TKE reduction and redistribution across spatial scales: spherical particles remove energy from large scales and reinsert it at small scales, while ellipsoids remove relatively less TKE from large scales and reinsert relatively more at small scales. Shape effects are far less evident in the statistics of particle rotation, which are very similar for ellipsoids and spheres. Comparing these with fluid enstrophy statistics, we find that particle rotation is dominated by velocity gradients on scales much larger than the particle characteristic length scales.

Key words: homogeneous turbulence, particle/fluid flow, suspensions

1. Introduction

Particle–turbulence interaction is central to many natural and industrial processes, such as sediment transport, plankton dynamics, combustion, and papermaking. Recent studies have led to significant advances in predicting the dynamics of small particles in high-Reynolds-number turbulence. These advances unite the classical theoretical work of Stokes, Jeffery and Batchelor with the new capabilities enabled by direct numerical simulation of turbulence. For particles smaller than the Kolmogorov length scale (η), simulations can include point particles whose coupling with the fluid phase

† Email address for correspondence: bellani@mech.kth.se

is described by the equations of Maxey & Riley (1983) for spheres, and Jeffery (1922) for ellipsoidal particles.

Numerical studies using this point-particle approach have shown that even moderate volume fractions ($\phi_v > 0.01\,\%$) of small particles can affect the fluid-phase turbulence (Squires & Eaton 1990; Elghobashi & Truesdell 1993; Elghobashi 2003; Ferrante & Elghobashi 2004). Particles modulate turbulence by altering both the production and dissipation of turbulent kinetic energy (TKE). This causes the TKE spectrum to pivot, showing increased energy at large wavenumbers and decreased energy at small wavenumbers. Such spectral pivoting has also been observed in laboratory studies (Schreck & Kleis 1993; Geiss *et al.* 2004; Yang & Shy 2005; Poelma, Westerweel & Ooms 2007).

The point-particle approach discussed above can no longer be applied when suspended particle sizes approach or exceed the Kolmogorov length scale (Balachandar & Eaton 2010). In such cases, there is no longer a scale separation between the turbulence and particle size scales. As the community works to address the more complicated case of large particles, there is a need for high-resolution laboratory measurements and numerical simulations to identify the mechanics of interphase coupling.

1.1. *Finite-size effects*

The analysis of finite-size particles is complicated because particles are large enough that the ambient turbulence cannot be approximated as simple (linear) shear (Qureshi *et al.* 2007). Furthermore, inertia might become important in the flow around the particle, so that the Stokes flow assumption might not be valid (e.g. see recent work of Calzavarini *et al.* 2012, and references therein).

Taylor-microscale-sized spherical particles have been investigated in detail using numerical simulations by Burton & Eaton (2005), Lucci, Ferrante & Elghobashi (2010) and Yeo *et al.* (2010), as well as by Bagchi & Balachandar (2003) for fixed particles. These simulations resolved the details of the three-dimensional unsteady wake around each particle as it responded to the ambient turbulent velocity field. Results showed that wakes were always in a transient state, and yielded larger average strain rates near the particles than would be found in a single-phase turbulent flow. This additional strain influences the TKE budget in two competing ways: increasing shear production of turbulence and increasing viscous dissipation. The work by Burton & Eaton (2005), Lucci *et al.* (2010) and Tanaka & Eaton (2010) all showed a net decrease in TKE.

For finite-size particles, the Stokes number no longer serves as a single parameter which collapses the dynamics, see for example the work by Eaton (1991), Kim, Elghobashi & Sirignano (1998), Ouellette, O'Malley & Gollub (2008), Saw *et al.* (2008), Xu & Bodenschatz (2008), Eaton (2009) and Lucci *et al.* (2010). This is because the effects of particle size and inertia become decoupled when particle diameter exceeds η, since the particle boundary directly alters the local velocity field through the no-slip and impermeability conditions. Indeed Lucci *et al.* (2010) show that particles with the same Stokes number but different sizes have different effects on turbulence. They find that separate parameters should be used to describe the particle inertia and size independently. Specifically, they suggest that total surface area is the most relevant parameter to describe size effects.

1.2. *Non-spherical particles*

The studies mentioned above focus on spherical particles, as do the vast majority of investigations. However, non-spherical particles are also of practical concern in

numerous scientific and engineering areas. The most common non-spherical particles considered in the literature are polymers. Results for long-chain flexible polymers include drag reduction and spectral pivoting (see Virk *et al.* 1967; Benzi *et al.* 2005; Liberzon *et al.* 2005). In this paper, we focus on the case of slightly aspherical non-deformable particles. These have been less well-studied, but are important for environmental engineering, e.g. sediment transport (Garcia 2008), pollen dispersion (Sabban & Van Hout 2011), and plankton dynamics (Jumars *et al.* 2009), as well as industrial applications, e.g. paper pulp (Lundell, Söderberg & Alfredsson 2010).

The dynamical behaviour of non-spherical particles is more complicated than that of spheres; for example, drag forces and torques depend on particle Reynolds number and instantaneous particle orientations. In quiescent flow, this effect can give rise to particle aggregation by differential settling, an effect that is not found for monodisperse spheres (Koch & Shaqfeh 1989). Compared to spheres, non-spherical particles also exhibit additional mechanisms that couple translation and rotation. These mechanisms include the minor-axis instability described by the 'tennis racket theorem' in solid mechanics, and orientation-dependent wake structures that can be significantly different from those of spheres (see Loth 2008, and references therein).

As a result of these complications, particle relaxation time scales differ between spherical and aspherical particles. Furthermore, aspherical particles have multiple orientation-dependent relaxation times, although for some particular orientation distributions a relaxation time scale can be defined (see Zhang *et al.* 2001). While particle relaxation time scales typically refer to translational motion, particles also have rotational relaxation times. Mortensen *et al.* (2007) have shown that the rotational response time of spheres is one third of the translational response time. For non-spherical particles the relaxation time strongly depends on the axis about which the particle rotates, complicating the definition of a single response time.

To investigate the rotational motion of non-spherical particles, one can use the analytical expressions of Jeffery (1922) which give the torque experienced by non-inertial ellipsoids in creeping shear flow. Based on this solution several numerical simulations of ellipsoidal particles in turbulent channel flows have been performed (e.g. Zhang *et al.* 2001; Mortensen *et al.* 2008*a*,*b*). Their simulations show that, in the near-wall region, ellipsoidal particles tend to align with the mean flow direction, whereas in the core of the channel the orientation tends to be more isotropic. The alignment in the near-wall region increases with increasing particle aspect ratio and inertia. Recent work of Lundell (2011) on inertial ellipsoids has shown that particle inertia can lead to chaotic rotational behaviour even in creeping flow.

When non-spherical particles are large, Jeffery's equations might fail to accurately describe their dynamics, due to significant inertial effects. There are currently very few studies on finite-size, inertial, non-spherical particles. Loth (2008) surveyed and organized a diverse collection of analytical and empirical results describing drag on non-spherical particles; the work of finding such relationships continues, e.g. in the recent direct numerical simulation (DNS) studies by El Khoury, Andersson & Pettersen (2010) and Zastawny *et al.* (2012). Turbulence in the ambient flow adds an additional layer of complexity by altering wake structure and the distribution of particle orientations. For the case of spherical particles, the influence of ambient turbulence on wake structure has been well-studied (e.g. Clamen & Gauvin 1969; Bagchi & Balachandar 2003, 2004; Moradian, Ting & Cheng 2009). To our knowledge, the dynamics of non-spherical finite-size particles freely moving in turbulence has not yet been experimentally investigated.

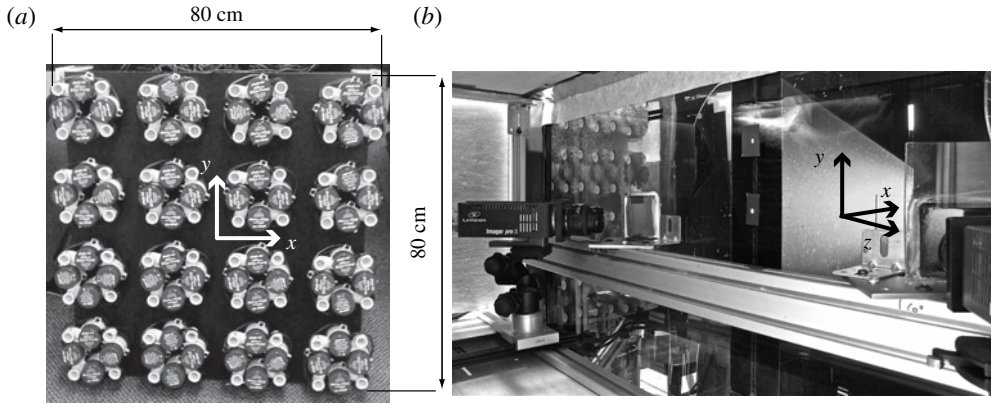

FIGURE 1. Experimental setup. Each of the 16 clusters seen in the pump array photo (*a*) has four synthetic jets, and the jets make an 8 × 8 Cartesian grid. (*b*) The origin and orientation of the coordinate system, and the laser sheet which defines the plane in which measurements are made.

1.3. *Present work*

To understand the dynamics of large, inertial, non-spherical particles in turbulent flow, we have developed an experimental technique with which we can simultaneously measure the angular velocity of arbitrarily shaped particles and the velocity field in the surrounding fluid. We use this technique to study the interaction of large (Taylor-scale) spherical and non-spherical particles in homogeneous isotropic turbulence (HIT). For both ellipsoids and spheres, we measure the effects of the particles on the turbulent flow (e.g. spectral pivoting) and the angular velocity statistics of the particles. We work with particles that are very near neutral buoyancy (specific gravity $= 1.02$) so that we can translate the results to particles of environmental interest: plankton and cohesive sediment aggregates ('flocs').

In § 2 the experimental facility, particles, and measurement methods are presented. In § 3 single-phase flow measurements are discussed. Results for turbulent modulation by particles are given in § 4 and statistics of particle rotation rates in § 5. In § 6 the results are discussed. Finally, conclusions are summarized in § 7.

2. Experimental method

2.1. *Turbulence tank*

Experiments are performed in a rectangular tank of dimensions 80 cm × 80 cm × 162 cm. The tank is filled with tap water, which is filtered to 5 microns and purified by a flow-through UV filter when experiments are not being run. The origin of the coordinate system is at the centre of the tank, z is oriented along the longest dimension of the tank, and y is vertical (as shown in figure 1*b*). The instantaneous velocity vector $\boldsymbol{U}(x, y, z, t) = (U, V, W)$ is defined so that U, V and W are aligned with the x-, y- and z-axes, respectively.

Turbulence is generated by two arrays of pumps located at both ends of the tank, in x–y planes at $z = 81$ cm and $z = -81$ cm. Each pump array has 64 individual pumps (see figure 1*a*) that are triggered in a random sequence. The pumps follow a randomizing algorithm developed by Variano & Cowen (2008) that maximizes the shear production of turbulence. The test section is in the tank centre, surrounding the

plane of symmetry between the pump arrays. This symmetry is a primary contributor to isotropy in the flow; the other main contributor is the use of a stochastic stirring pattern. By preventing mean velocity gradients from persisting, the stochastic stirring greatly reduces tank-scale circulation. Such circulation is an unwanted effect of any turbulence generation method. By reducing the tank-scale circulation, the flow we measure has a mean velocity close to zero.

In addition to large-scale isotropy, this turbulence tank has a large homogeneous region in the tank centre. The size of this region is estimated as 30 cm × 30 cm × 30 cm (see Variano & Cowen 2008; Bellani 2011 for more details). This region is much larger than the turbulent integral length scale (≈7 cm), which means that the flow statistics measured there will be unbiased by spatial gradients, even in the most energetic turbulent events. Furthermore, particle statistics measured in this test section will accurately represent the effects of homogeneous isotropic turbulence, and not include the signature of flows in other regions of the tank. This can only be accomplished with a large homogeneous region because particle motion depends in part on the history of the flow. Any particle in the measurement domain will have already travelled through a large region of homogeneous turbulence identical to that in the test section, and thus the motion we measure will reflect this flow exclusively.

The Reynolds number achieved here is $Re_\lambda \approx 270$ (defined with respect to the Taylor microscale) or equivalently $Re_\Lambda \approx 1500$ (defined with respect to the integral length scale). This Reynolds number is high enough to establish a clear inertial subrange in the two-point fluid velocity statistics. The details of the flow will be discussed further in § 3.

2.2. *Particles*

Particles are made of a hydrogel that is 99.5 % water (Agarose 5 g l^{-1}), and they are manufactured by injection moulding. This particular hydrogel solution has been chosen so that particles are near neutrally buoyant and have a refractive index very close to the surrounding water. The index of refraction is 1.337 at 20 °C, and the density $\rho_p = 1020$ kg m^{-3}.

Two shapes are considered here: spheres of diameter $d_s = 8$ mm, and prolate ellipsoids whose polar and equatorial axes are $l_e = 16$ and $d_e = 8$ mm, respectively. These particle sizes were chosen to correspond to eddy sizes in the inertial subrange. While the particles do not follow Stokes flow in our experiments, we compute a Stokes-based response time as a point of reference. Particle response time can be defined in two ways, both of which use the Stokes model for drag on a sphere in creeping flow. The first method considers that particles in a uniform steady flow are predicted to exponentially approach steady-state velocity with characteristic time scale $\tau_{p(1)} = \rho_p d_s^2/18\mu$, where μ is fluid viscosity. The second method is to normalize the particle terminal velocity (in a quiescent fluid) by gravitational acceleration, giving $\tau_{p(2)} = (\rho_p - \rho_f)d_s^2/18\mu$, where ρ_f is the fluid density. The two definitions become equivalent when $\rho_p \gg \rho_f$, but diverge notably for near-neutrally buoyant particles. Herein we use the first definition, and note that for neutrally buoyant particles, $\tau_{p(1)}$ is the time scale of exponential approach to the ambient fluid velocity, while $\tau_{p(2)} = 0$.

The spherical particles have $\tau_{p,s} = \rho_p d_s^2/18\mu = 3.64$ s. The Stokes-based response time of the ellipsoidal particles is computed using the expression derived by Zhang *et al.* (2001) for randomly oriented ellipsoidal particles:

$$\tau_{p,e} = \tau_{p,s}\lambda\frac{\log(\lambda + \sqrt{\lambda^2 - 1})}{\sqrt{\lambda^2 - 1}}, \tag{2.1}$$

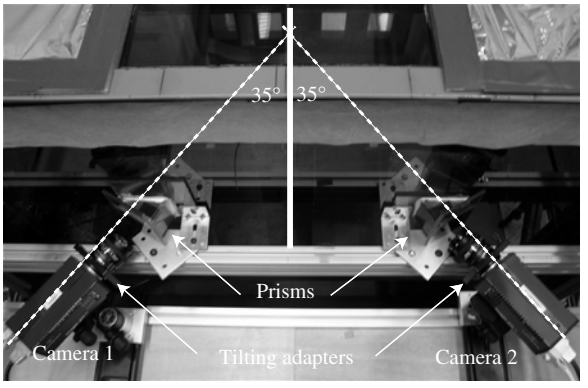

FIGURE 2. Imaging setup for stereoscopic PIV. Solid line indicates laser light-sheet.

where $\lambda = l_e/d_e$ is the particle aspect ratio and $\tau_{p,s}$ is the relaxation time of a sphere of diameter d_e. In this case, $\lambda = 2$, which gives $\tau_{p,e} = 1.5\tau_{p,s} = 5.46$ s. For large particles that do not passively follow the flow, the slip velocity (and thus particle Reynolds number) can be defined in a variety of ways (e.g. see Xu & Bodenschatz 2008; Lucci *et al.* 2010; Calzavarini *et al.* 2012). We compute particle Reynolds number using the fluid-phase turbulent velocity scale $u' = (u_{rms} + v_{rms} + w_{rms})/3$ (as in Xu & Bodenschatz (2008)), and the particle diameter. For the ellipsoidal particles, we use the diameter of the sphere that has the same average Stokesian response time as an ensemble of randomly oriented ellipsoids (Clift, Grace & Weber 1978). The corresponding values of particle Reynolds number are reported in table 2 below. If particles are not entirely passive, then this velocity scale may be an overestimate; we investigate the issue of particle slip velocity in Bellani & Variano (2012).

2.3. *Measurement technique and phase discrimination*

Simultaneous fluid- and particle-phase velocity measurements are performed using stereoscopic particle-image velocimetry (PIV). Two cameras (Imager PRO-X, 1600 × 1200 pixels, both fitted with a 50 mm Nikkor lens and Scheimpflug/tilt adapter) view a 1 mm thick laser light sheet, capturing a measurement volume of 14 cm × 8 cm × 0.1 cm centred in the tank. They view the measurement area from opposite sides, each at an angle of 35° relative to the laser's forward-scatter direction. To avoid image distortion by the air–glass–water interface at the tank walls, two 35° prisms filled with water are attached to the walls (see figure 2).

The images we collect simultaneously capture the particles, tracers embedded within the particles, and passive tracers within the fluid phase (10 μm silver-coated glass spheres). A particular challenge in this setup is to match the imaged intensity of the fluid-phase tracers and the tracers embedded in the particles. This is accomplished through careful choice of the viewing angle (35°), viewing orientation (forward-scatter), tracer size, tracer coating, laser power, camera aperture, and angle of linear polarizing filters. Figure 3(*a*) shows a typical image where both fluid tracers and a large particle are visible. Differences in background intensity allow us to isolate the particle phase from the fluid phase, and perform analysis separately on each phase (see figure 3*b*).

Stereoscopic PIV applied to the images provides two-dimensional arrays of three-dimensional velocity vectors, with 61 × 109 measurement points equally spaced by

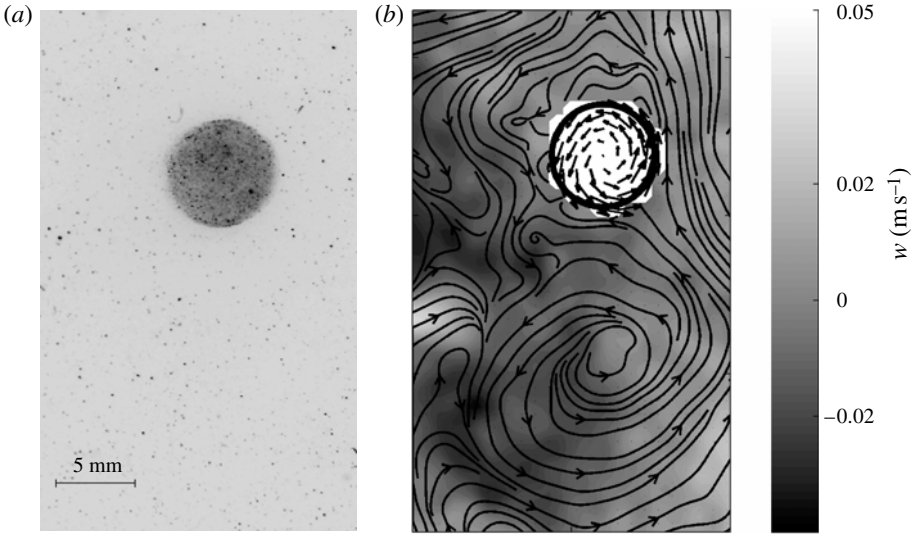

FIGURE 3. (*a*) Large spherical particle moving freely in turbulence. The tracers embedded in the particle can be distinguished above the higher background intensity in the particle. (*b*) Output of PIV measurements in the fluid and the particle phase. In the fluid phase, the grey scale indicates the magnitude of the out-of-plane velocity component, whereas the streamlines are based on the in-plane components. In the particle, arrows show velocities measured by following tracers embedded in the solid body.

1.3635 mm grid sizes. This grid spacing is approximately equal to the laser sheet thickness. Statistics of the flow field are computed from at least 510 independent velocity fields acquired at 0.5 Hz (which corresponds to 17 min or 378 eddy turnover times). Statistics for the particle-laden cases are computed from 680 vector fields; this increase relative to the single-phase case compensates for reduced fluid-phase data when particles are present. For all cases, we confirm that the amount of data is sufficient to provide converged statistics.

We create particle suspensions by dispersing 1.5 l of particles in the 1037 l volume of the turbulence tank. This gives a volume fraction of $\phi_v = 0.14\,\%$. For this volume fraction, the suspension regime is considered dilute, which means that particle–particle interactions can be neglected (Elghobashi 1994). We use the same volume fraction for both spheres and ellipsoids, thus the number density of ellipsoids is half that of the spheres, and the total surface area of spheres in the tank is 17 % larger than that for ellipsoids.

2.4. *Rotation measurements*

We calculate the angular velocity of particles from the vector field within each particle and the equation of solid-body motion. The angular velocity $\boldsymbol{\Omega}$ can in principle be determined from the velocity measured at any two locations $\boldsymbol{X}_M$ and $\boldsymbol{X}_N$ within a particle:

$$\boldsymbol{U}_N = \boldsymbol{U}_M + \boldsymbol{\Omega} \times (\boldsymbol{X}_N - \boldsymbol{X}_M). \tag{2.2}$$

Stereoscopic PIV provides the necessary values $\boldsymbol{U}_M$, $\boldsymbol{U}_N$, $\boldsymbol{X}_M$ and $\boldsymbol{X}_N$. However, since all points M and N are located in the same plane ($z = 0$), (2.2) is over-determined in Ω_z and under-determined in Ω_x and Ω_y. Hence, to solve the system we need at

least three non-aligned points. By including a third point P in the analysis, all three components of $\boldsymbol{\Omega}$ can be determined according to the system

$$\begin{pmatrix} U_N \\ V_N \\ W_N \\ U_M \\ V_M \\ W_M \end{pmatrix} = \begin{pmatrix} U_M \\ V_M \\ W_M \\ U_P \\ V_P \\ W_P \end{pmatrix} + \begin{pmatrix} 0 & 0 & -(Y_N - Y_M) \\ 0 & 0 & -(X_N - X_M) \\ (Y_N - Y_M) & (X_N - X_M) & 0 \\ 0 & 0 & -(Y_M - Y_P) \\ 0 & 0 & -(X_M - X_P) \\ (Y_M - Y_P) & (X_M - X_P) & 0 \end{pmatrix} \cdot \begin{pmatrix} \Omega_x \\ \Omega_y \\ \Omega_z \end{pmatrix}. \quad (2.3)$$

Solving this equation gives one measurement of Ω_x, one of Ω_y, and four measurements of Ω_z; we take the mean of the four estimates as our estimate of Ω_z.

For each particle measured in this experiment, we obtain the velocity of significantly more than three interior points. These additional data are used to improve precision and accuracy in the measured $\boldsymbol{\Omega}$. We do this by calculating a value of $\boldsymbol{\Omega}$ using every possible triplet of points M, N and P where PIV data were available. From this ensemble of estimates of Ω we take the median as the best estimate of Ω, and the standard deviation as the uncertainty on Ω. A global optimization based on singular-value decomposition was also tested, and performed less well when compared to known rotation values. These results, and the related benchmark tests, are discussed in work in preparation by three of the present authors (Meyer, Collignon and Variano).

We also note that this measurement technique is optimized for computing the rotational, rather than translational, component of particle motion. Future extensions of this technique will allow analysis of translation statistics such as slip velocities and particle Reynolds number.

3. Single-phase measurements

We begin by investigating a single-phase turbulent flow without suspended particles, which will serve as a base case. The velocity statistics measured in this single-phase flow are summarized in table 1. The probability density function (p.d.f.) of fluctuating velocities is shown in figure 4. These results indicate large-scale isotropy, as the p.d.f. is not skewed and all three velocity components have the same variance. Figure 4 also shows the super-Gaussian behaviour of fluctuating velocities often seen in turbulence (e.g. Tsinober 2004). The spatial distribution of velocity statistics (not shown) demonstrates homogeneity in x and y.

We decompose velocity into a temporal mean $\overline{\boldsymbol{U}}(\boldsymbol{x})$ and a fluctuating component $\boldsymbol{u}'(\boldsymbol{x}, t)$, with the magnitude of the turbulent velocity fluctuations defined as $\boldsymbol{u}_{rms}(\boldsymbol{x}) = \sqrt{\overline{\boldsymbol{u}'(\boldsymbol{x}, t)^2}}$. The overbar denotes the linear time-average operator, and herein is considered equivalent to the expectation value $\langle\cdot\rangle$ by ergodicity.

The mean flow is one order of magnitude smaller than the turbulent velocity fluctuations. Quantitatively, we compare the mean flow kinetic energy $M^2 = \overline{U}^2 + \overline{V}^2 + \overline{W}^2$ to the turbulent kinetic energy (TKE) $k = \frac{1}{2}\overline{(u_{rms}^2 + v_{rms}^2 + w_{rms}^2)}$ and compute the quantity $I = M/\sqrt{2k} = 0.079 \pm 0.053$.

Longitudinal variations in fluctuating velocities are used to calculate two-point statistics, from which we find dissipation rate, integral length scale, and power spectra.

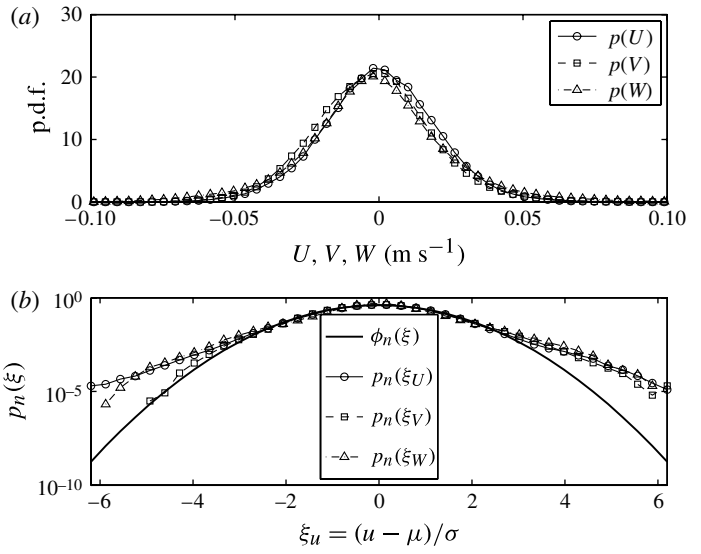

FIGURE 4. Probability density functions of the U (○–), V (□- -) and W (△· -) velocity components in dimensional (a) and normalized (b) form. In (b), the solid line is a normal distribution $\phi_n = (1/\sqrt{2\pi})\mathrm{e}^{-\xi^2/2}$, and the y-axis has a logarithmic scale to highlight the behaviour of the tails.

Mean flow magnitude	$M \equiv \sqrt{\overline{U}^2 + \overline{V}^2 + \overline{W}^2}$	0.3 ± 0.2 ($\times 10^{-2}$ m s^{-1})
Velocity fluctuations in x	$\sqrt{\overline{u_{rms}^2}}$	2.02 ± 0.04 ($\times 10^{-2}$ m s^{-1})
Velocity fluctuations in y	$\sqrt{\overline{v_{rms}^2}}$	2.05 ± 0.04 ($\times 10^{-2}$ m s^{-1})
Velocity fluctuations in z	$\sqrt{\overline{w_{rms}^2}}$	2.50 ± 0.06 ($\times 10^{-2}$ m s^{-1})
Turbulent kinetic energy	$k = \frac{1}{2}(\overline{u_{rms}^2} + \overline{v_{rms}^2} + \overline{w_{rms}^2})$	7.2 ± 0.1 ($\times 10^{-4}$ m^2 s^{-2})
Mean flow to turbulence ratio	$I = M/\sqrt{2k}$	0.079 ± 0.053
Longitudinal integral length scale	Λ_x	71.7 ($\times 10^{-3}$ m)
Taylor microscale	λ_x	12.2 ($\times 10^{-3}$ m)
Eddy turnover time	$T = \Lambda_x/u_{rms}$	3.3 (s)
Dissipation rate (from λ_x)	$\epsilon = 15\nu\ u_{rms}^2/\lambda_x^2$	4.83 ($\times 10^{-5}$ m^2 s^{-3})
Kolmogorov time scale	$\tau_\eta = (\nu/\epsilon)^{1/2}$	0.14 (s)
Kolmogorov length scale	$\eta = (\nu^3/\epsilon)^{1/4}$	0.38 ($\times 10^{-3}$ m)
Reynolds number (based on Λ_x)	$Re_L = (\Lambda_x u_{rms})/\nu$	1577
Reynolds number (based on λ_x)	$Re_\lambda = (\lambda_x u_{rms})/\nu$	269

TABLE 1. Flow statistics from single-phase measurements. The parameters denoted by the overbar are average quantities over the entire measurement domain, and the intervals correspond to the 95 % confidence intervals. The integral length scale and the Taylor microscale are computed from the longitudinal two-point correlation, from which the dissipation rate and the Kolmogorov scales are computed using the definitions given in Pope (2000). ν, kinematic viscosity (μ/ρ, where μ is dynamic viscosity).

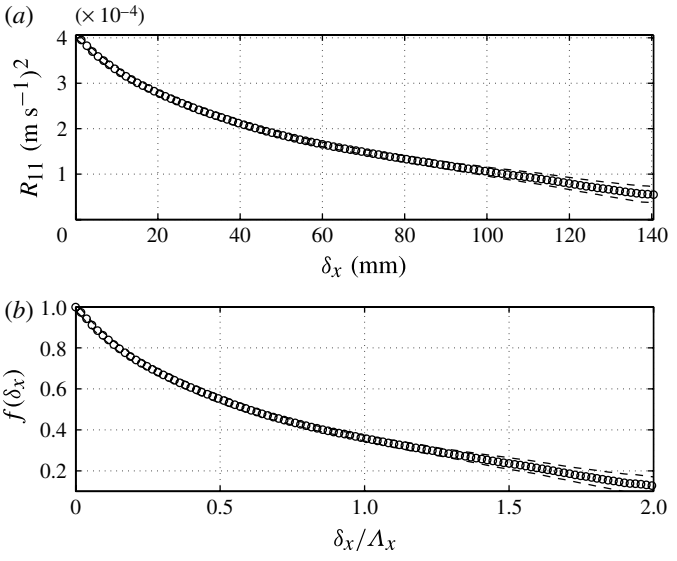

FIGURE 5. Longitudinal autocovariance R_{11} (a) and correlation function f (b). The dashed line shows the standard error.

Central to these analyses is the autocovariance:

$$R_{11}(\boldsymbol{x}, t, \delta_x) = \langle u'(\boldsymbol{x}, t) u'(\boldsymbol{x} + \delta_x, t) \rangle, \tag{3.1}$$

where δ_x is a variable separation in x. The average of R_{11} over space is shown in figure 5(a). By introducing the autocorrelation function $f(\delta_x) = R_{11}(\delta_x)/u_{rms}^2$ (shown in figure 5b) we can compute the integral length scale $\Lambda_x = \lim_{L\to\infty} \int_0^L f(\delta_x)\, \mathrm{d}\delta_x$. Here L is limited by the length of the measurement domain, and is equal to 140 mm. However, for the single purpose of computing the integral length scale we have extrapolated the values of f to $\delta_x = 420$ mm using an exponential fit to the last third of the data, so that the integral length scale $\Lambda_x = 71.7$ mm is estimated by integrating over a domain of $\sim 6\Lambda_x$.

The Taylor length scale λ_x and dissipation rate ϵ are related by $\epsilon = 15\nu u_{rms}^2/\lambda_x^2$ in high-Reynolds-number homogeneous isotropic turbulence. We determine these values in two ways. First, we calculate λ_x from the autocorrelation function as $\lambda_x = [-0.5 f''(0)]^{-0.5}$. Second, we compute ϵ from the slope of the second-order structure function. The two approaches show a good agreement, giving $\epsilon \approx 0.5$ cm^2 s^{-3}. The turbulent scales that follow from ϵ are summarized in table 1.

Following Pope (2000), we can define the longitudinal wavenumber spectrum $E_{11}(\kappa)$ as:

$$E_{11}(\kappa) = \frac{2}{\pi} u_{rms}^2 \int_0^\infty f(\delta_x) \cos(\kappa \delta_x)\, \mathrm{d}\delta_x. \tag{3.2}$$

Particular care is needed when computing spectra from a window of finite size (length L) such as in PIV measurements (where $\delta_x \in [0, L]$). This is because spectral distortion can occur due to side-lobe leakage (Bendat & Piersol 2010). In order to suppress that, before computing the spectrum according to (3.2), the correlation function is premultiplied by a tapering function $a_t(\delta_x)$ that declines linearly from $a_t(0) = 1$

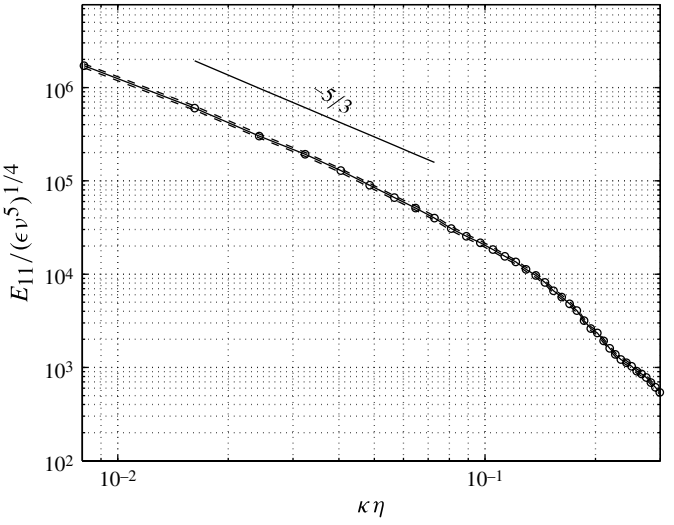

FIGURE 6. Longitudinal spectrum calculated using (3.3). The dashed lines show the magnitude of the random error for the spectral estimate.

to $a_t(L) = 0$. Thus E_{11} is computed as:

$$E_{11}(\kappa) = \frac{2}{\pi} u_{rms}^2 \int_0^L a_t(\delta_x) f^c(\delta_x) \cos(\kappa \delta_x)\, \mathrm{d}\delta_x, \tag{3.3}$$

where $f^c(\delta_x)$ is the circular correlation function. From a mathematical point of view, (3.3) is equivalent to computing the spectrum from:

$$E_{11}(\kappa) = \frac{1}{N_t} \sum_{i=1}^{N_t} \left(\frac{1}{L} X_i^*(\kappa) X_i(\kappa) \right), \tag{3.4}$$

where $X_i(\kappa)$ is the Fourier transform of $u'(x, t_i)$. Although estimating the spectra from (3.4) is computationally more efficient, it requires the interpolation of the missing vectors in the velocity field, which can cause significant distortion if the number of interpolated vectors is larger than 10 % of the total (see Poelma, Westerweel & Ooms 2006). This is usually not a problem for single-phase measurements, where typically the number of missing vectors is lower than 5 %; however the distortion can become significant when analysing the particle-laden flow, due to the large gaps in the fluid-phase velocity fields created by the particles (in our measurements on the order of 10 % of vectors are blocked by particles). Instead, computing the two-point correlation does not require any interpolation of the velocity fields, thus here we compute the spectra using (3.3).

The one-dimensional power spectrum is shown in figure 6. The spectrum shows a power-law decay with $-5/3$ slope which extends for more than one decade. The exponential decay range begins near $\kappa\eta < 0.1$, as predicted by the K41 theory for $Re_{\lambda_x} = 270$ (see the model spectrum in Pope 2000). Uncertainty in the spectrum will be important when evaluating the effect of particles. This can be quantified by the relative random error $e_r = \sqrt{1/N_t}$, where $N_t = 510$ in our case giving a random error of $\sim$5 %.

	Single phase	Spheres	Ellipsoids
Particle aspect ratio	—	1	2
Volume fraction ϕ_v	0	0.0014	0.0014
$(d_p, l_p)/\eta$	—	21, 21	21, 42
$(d_p, l_p)/\lambda_x$	—	0.65, 0.65	0.65, 1.3
$(d_p, l_p)/\Lambda_x$	—	0.11, 0.11	0.11, 0.22
τ_p/τ_η	—	26	39
τ_p/T	—	1.1	1.6
$Re_p = u' d_p/\nu$	—	175	229

TABLE 2. Definition of the three experimental cases and key governing geometric and kinematic parameters.

	Single phase	Spheres	Ellipsoids
Mean flow magnitude, M ($\times 10^{-2}$ m s^{-1})	0.3 ± 0.2	0.5 ± 0.2	0.4 ± 0.2
TKE, k ($\times 10^{-4}$ m^2 s^{-2})	7.2 ± 0.1	6.2 ± 0.1	7.0 ± 0.1
TKE variation relative to single phase (%)	0%	−15 %	−3 %
u_{rms} ($\times 10^{-2}$ m s^{-1})	2.01	1.94	2.02
v_{rms} ($\times 10^{-2}$ m s^{-1})	2.05	1.87	2.02
w_{rms} ($\times 10^{-2}$ m s^{-1})	2.5	2.29	2.44
Skewness of u	0.01	0.03	0.16
Skewness of v	0.15	0.23	0.05
Skewness of w	0.10	0.26	0.27
Flatness of u	3.80	3.74	4.75
Flatness of v	3.63	3.96	3.68
Flatness of w	4.62	5.43	5.59

TABLE 3. Summary of single-point fluid-phase velocity statistics for the three cases.

4. Turbulence modification by particles

Here we compare the dynamics of particle-laden flows with the single-phase flow. A key goal is to measure the effect of particle shape on turbulence modulation. Thus we hold volume and mass fraction of the suspension constant while varying the particle shape. Physical and geometrical characteristics of the particles have been described in § 2.2. A summary of the governing parameters for the three cases (single phase, spherical and ellipsoidal particle-laden) is shown in table 2.

4.1. *Effect of particles on one-point statistics*

In table 3 the turbulent statistics of the fluid phase are shown for both particle suspensions and single-phase flow. Homogeneity and isotropy of the flow are not notably affected by the particles. Most notably, the turbulent kinetic energy (averaged over space) is decreased in both particle-laden cases. Spherical particles provide a 15 % reduction of TKE, while only a 3 % reduction is observed for ellipsoidal particles. The TKE modulation observed in the measurement volume is due to the integrated effects of particles throughout the stirred tank. That is, particles affect production and dissipation of TKE everywhere, which in turn alters the TKE flux into the measurement volume. Thus the results reported herein are for a range of turbulent Reynolds numbers (Re_T), albeit a narrow range due to the tank's high degree of spatial

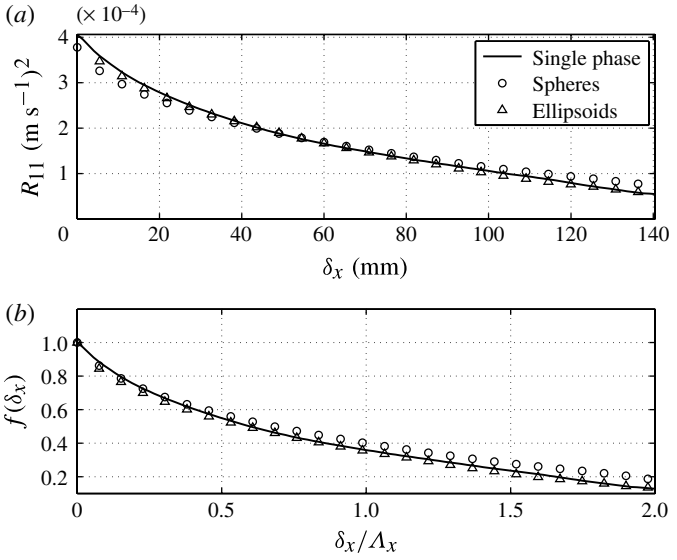

FIGURE 7. Longitudinal autocovariance R_{11} (*a*) and correlation function f (*b*) for the three cases. For clarity, only every fourth data point is shown for the particle-laden cases.

homogeneity. Future measurements can more precisely isolate single values of Re_T by observing spatial or temporal decay patterns, as discussed in Poelma *et al.* (2007) and Lucci *et al.* (2010).

One advantage of the experimental method used herein is that TKE production is spread over a wide range of spatial scales. This prevents the turbulence generation mechanism from obscuring the effects of turbulence modulation by suspended particles, which is a common risk in DNS of steady-state turbulence, as discussed in Lucci *et al.* (2010).

4.2. *Two-point statistics and spectra*

More information about the structure of turbulence can be obtained by considering the velocity autocorrelation function and power spectrum. These are computed following the procedure described in § 3, and are shown in figures 7 and 8.

Figure 7(*a*) shows the longitudinal two-point correlation in dimensional form so that the difference in energy between the three cases can be observed. As already discussed, both particle-laden cases have a lower variance than for the single phase. The autocorrelation function is shown in figure 7(*b*). The difference between these curves can be more easily evaluated by transforming them to power spectra.

The longitudinal power spectra are shown in figure 8; for both cases, particle-laden flow has less TKE than single-phase turbulence at small wavenumbers, and more at large wavenumbers. Of these two effects, the TKE deficit at small wavenumbers is greater in magnitude than the excess TKE at large wavenumbers (note logarithmic axis). This results in flatter slopes for both particle-laden cases than for single-phase flow. Such pivoting has also been observed in experiments by Schreck & Kleis (1993), Geiss *et al.* (2004), Yang & Shy (2005) and Poelma *et al.* (2007). We interpret the observed pivoting using the phenomenology described by Lucci *et al.* (2010) and Tanaka & Eaton (2010). This would predict that both particle types alter the turbulent cascade by generating shear at particle surfaces. In our data, the two particle

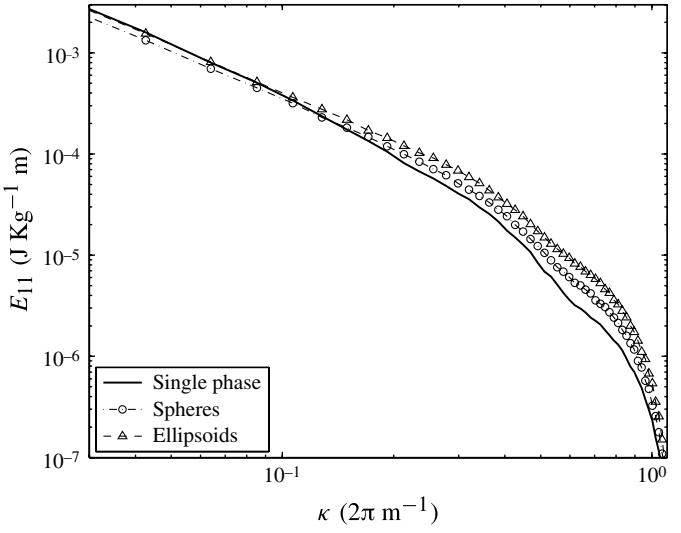

FIGURE 8. Energy spectrum for single-phase (solid line), spherical particles (○) and ellipsoidal particles (△).

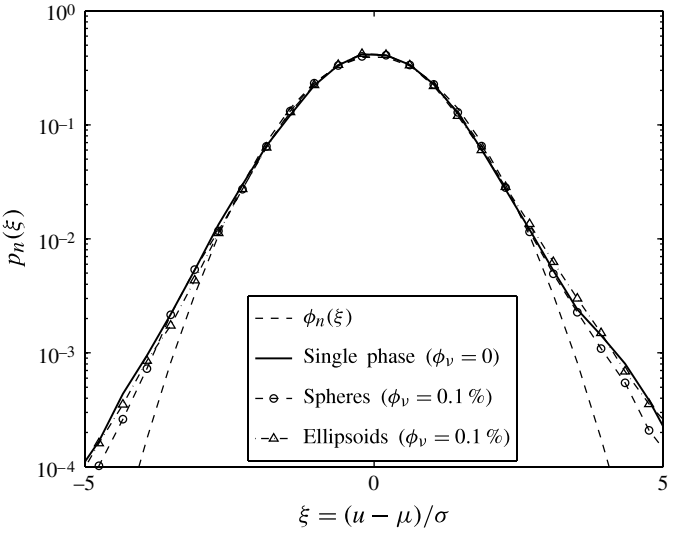

FIGURE 9. Fluid-phase velocity p.d.f.s for the three cases and the normal distribution (dashed line)

types appear to have different effects on the turbulent cascade, and thus the turbulent spectrum. Ellipsoids appear to remove energy from large-scale motions and re-inject almost all of it at smaller scales. Spheres apparently remove even more energy from large scales, and inject relatively less back into small scales. This results in the significant TKE decrease observed in the spherical-particle case.

Another useful comparison can be made by looking at the velocity p.d.f.s (figure 9). Here the main difference occurs in the tails, for $|\xi| > 3$, as the tails for the spherical

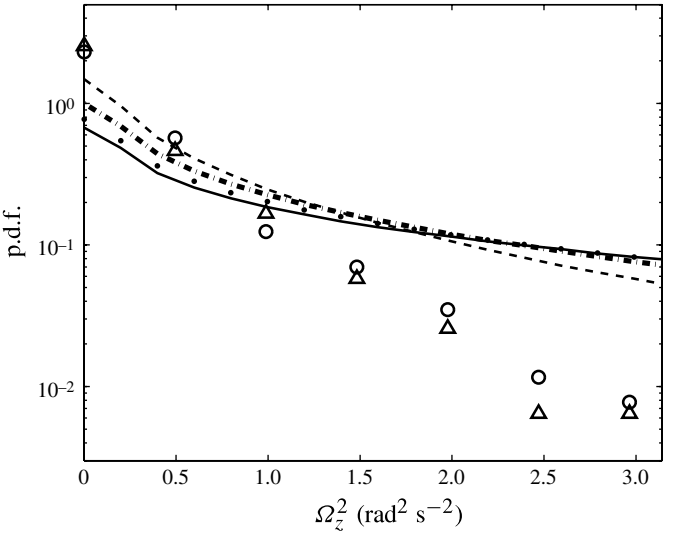

FIGURE 10. Particle rotation p.d.f.s (symbols) and fluid enstrophy p.d.f.s (lines). Ω_z^2 is shown for spheres (○) and for ellipsoids (△). ω_z^2 computed from velocity fields filtered at λ_c: 1.33 mm (−); 4 mm (·); 8 mm (− · −); 16 mm (− −).

	μ (rad^2 s^{-2})
ω_z^2 filtered at $\lambda_c = 1.3$ mm	$11.11 \leqslant 11.14 \leqslant 11.17$
ω_z^2 filtered at $\lambda_c = 4$ mm	$5.67 \leqslant 5.68 \leqslant 5.69$
ω_z^2 filtered at $\lambda_c = 8$ mm	$3.11 \leqslant 3.12 \leqslant 3.13$
ω_z^2 filtered at $\lambda_c = 16$ mm	$1.30 \leqslant 1.31 \leqslant 1.32$
Ω_z^2 spheres	$0.26 \leqslant 0.31 \leqslant 0.34$
Ω_z^2 ellipsoids	$0.18 \leqslant 0.23 \leqslant 0.28$

TABLE 4. Expected values (μ) of Ω_z^2 and $\omega_z^2/4$ with their respective 95 % confidence intervals.

particle case seem to decay slightly faster than the others. This means that rare, high-speed events are dampened by the presence of spherical particles, far more than by ellipsoids, which instead tend to be closer to the single-phase measurements.

5. Particle rotation

We compute particle rotation statistics from 819 independent measurements of spheres and 513 of ellipsoids. For each measurement we determine the instantaneous rotation rate vector $\boldsymbol{\Omega} = (\Omega_x, \Omega_y, \Omega_z)$ as explained in § 2.4. Statistics of $\boldsymbol{\Omega}$ shown on table 4 and figure 10 are very similar for both particle types, which is surprising given their different impact on fluid-phase turbulence.

To better understand the cause of observed $\boldsymbol{\Omega}$ values, we compare particle rotation and fluid velocity gradients. We compute fluid enstrophy ω^2 (where $\boldsymbol{\omega} = \boldsymbol{\nabla} \times \boldsymbol{U}$) from the PIV data and compare its statistics to that of particle rotation rates. Owing to their

finite size, we can expect that particles do not respond to velocity gradients smaller than their characteristic dimensions, hence it is necessary to analyse fluid enstrophy at different length scales. Here we obtain enstrophy statistics from velocity fields smoothed with a Gaussian filter with four cutoff wavelengths: $\lambda_c = 1.3$ mm (spatial resolution of the raw data), 4 mm (half particle diameter), 8 mm (sphere diameter and ellipsoid minor axis), and 16 mm (ellipsoid major axis). Planar PIV allows us to extract only one component of the fluid enstrophy (ω_z^2), thus we compute this and compare it to the z-component of particle rotation (Ω_z).

The means of Ω_z^2 and $\omega_z^2/4$ (to keep notation simple, we skip the factor of 4 from now on, so all statistics of ω_z^2 are intended to be statistics of $\omega_z^2/4$), with their respective 95 % confidence intervals, are shown in table 4. The mean and standard deviation of ω_z^2 decrease monotonically as the cutoff wavelength increases but are higher than the average rotation rates of both spherical and ellipsoidal particles. In figure 10 we plot the p.d.f.s of Ω_z of both spherical and ellipsoidal particles together with the p.d.f.s of the fluid enstrophy computed from the filtered velocity fields. The similar rotational dynamics of the two types of particle shapes is evident from this plot. Interestingly, p.d.f.s for both particle shapes do not match the p.d.f. of fluid enstrophy computed from velocity fields filtered at the particle scale. To match the curves, we would need fluid enstrophy computed for velocity fields smoothed with a filter with a much larger wavelength than the particle dimensions.

Reduced r.m.s. of particle rotation rates compared to r.m.s. of fluid rotation rates has been reported in a recent numerical study by Zhao & Andersson (2011) for small heavy particles. They showed that this reduction is due to two effects: preferential concentration in low-vorticity regions and the time-lagged response of the particles to ambient flow. Either of these two effects is possible in our flow, as well as a third: the large size of the particles effectively filtering out the effect of small-scale high-vorticity fluid motion, as discussed above. It is not yet known whether large near-neutrally buoyant particles can show preferential concentration, and the current study can neither confirm nor rule out the presence of this effect. The effect of time lag is certainly present for the flow measured here. To examine this effect, we compute the particle rotational relaxation time and compare it to the characteristic time scale of vortices at the particle scale.

We estimate the particle rotational relaxation times τ_r as one third of the relaxation time for translation (see Zhao & Andersson 2011, for the derivation of τ_r). This yields $\tau_r = 1.21$ s for spheres and $\tau_r = 1.76$ s for ellipsoids. The time scale of vortices at the particle size is computed as $\tau(d_p) = (d_p^2\epsilon^{-1})^{1/3}$ and equals 1.09 s based on the sphere diameter and 1.72 s based on the ellipsoid polar diameter. Thus the time scales of fluid motion at the particle scale are very similar to the particle rotational relaxation time, and about one third of the particle translational relaxation time. This relatively slow reaction time implies that particle rotation is set by fluid motions at large spatial scales, as these motions have time scales similar to the particle relaxation time. In contrast, fluid motions at the particle scale do not persist long enough for the particle to come to equilibrium with their (relatively higher) vorticity.

6. Discussion

Recent studies on large spherical particles suggest that turbulence modulation is governed by the particle inertia and the total wetted surface area in the particle phase (Lucci *et al.* 2010; Tanaka & Eaton 2010; Lucci, Ferrante & Elghobashi 2011). The data presented in the previous sections suggest that shape can also play an important

role in turbulence modulation. We find it more likely that the difference in TKE reduction between ellipsoidal and spherical particles is caused by shape-dependent differences in particle dynamics, than by relatively small differences in total surface area or particle inertia in our experimental setup.

To understand the mechanism of shape sensitivity in turbulence modulation, we consider two possible explanations for the observed 15 % reduction in TKE by spheres, which far exceeds the 3 % reduction caused by ellipsoids. Hypothesis (i) is that ellipsoids tend to align preferentially with the principal axis of fluid strain, in such a way that they cause very little additional dissipation relative to the single-phase case. Hypothesis (ii) is that ellipsoids produce wakes and that these wakes are more energetic than those produced by spheres, such that ellipsoids increase the total amount of TKE production in a flow more than spheres do.

Inspection of the p.d.f. tails in figure 9 lends support to hypothesis (i), as it shows that extreme velocity events are not affected by ellipsoids, but are significantly damped by spheres. We consider this indicative of a process in which spheres cause additional dissipation, rather than ellipsoids causing additional production. However, preliminary data on fluid statistics conditioned on distance to the particle boundary show that TKE enhancement near the particle surface is greater in the case of ellipsoids than spheres, thus supporting hypothesis (ii). A detailed analysis of the flow gradients around the particles would advance these lines of inquiry by allowing us to more directly quantify the production and dissipation mechanisms present in particle wakes. This requires data at a finer spatial resolution than presented here, which instead has been optimized to measure global effects on turbulence modulation. Hence, the analysis of velocity gradients is left as future work.

The observation that particle shape has no measurable effect on particle rotation statistics is rather surprising. We explain it through the evidence that spheres and ellipsoids respond primarily to velocity gradients on scales much larger than their characteristic size. This implies that the particles are not responding to those scales that include shape-dependent local flow modifications. Further analysis of this issue will include forthcoming data that capture Lagrangian time series of particle rotation.

7. Conclusions

We report an experimental technique with which we simultaneously measure rotation rates of arbitrarily shaped particles and the velocity field in the surrounding fluid. This provides experimental data heretofore only available from DNS, particularly the particle rotation rates.

We establish a turbulent flow which is homogeneous and isotropic at high Reynolds number, and use this to understand the effects of particles suspended in the flow. The main goal of this work is to evaluate the effect of particle shape on turbulence–particle coupling. To this end, we measure both spherical particles and prolate ellipsoids with aspect ratio 2. For relevance to environmental applications, we use particles that are nearly neutrally buoyant and roughly equal in size to the Taylor microscale, i.e. in between the largest and smallest scales in the turbulent inertial subrange.

We find that spherical particles provide a 15 % TKE reduction relative to a flow without particles. This is a much larger impact than shown by the ellipsoidal particles, which cause a reduction of only 3 %, despite having the same volume fraction and nearly the same total surface area as spheres. The reason for this lies in the details of the flow near the particle surface, which lead to changes in production and dissipation of TKE, as well as redistribution of TKE across scales. Our spectral analysis indicates

that spheres remove TKE from large scales and reinsert significantly less at smaller scales, while ellipsoids shift TKE from large scales to small scales without much net loss. Ellipsoid preservation of TKE may indicate that they have a negligible effect on production and dissipation, or that their additional production and dissipation are nearly in balance. Fluid-phase velocity p.d.f.s indicate that ellipsoids do not alter the likelihood of extreme velocity events, while spheres make such occurrences less frequent.

We compute statistics of particle rotation rates and compare these to fluid enstrophy statistics, from which two main conclusions are evident: (i) rotation rate statistics of spheres and ellipsoids are nearly equivalent; (ii) for the parameters studied here, rotational dynamics of spheres and ellipsoids are determined by velocity gradients occurring on a larger scale than their physical size.

REFERENCES

BAGCHI, P. & BALACHANDAR, S. 2003 Effect of turbulence on the drag and lift of a particle. *Phys. Fluids* **15** (11), 3496–3513.

BAGCHI, P. & BALACHANDAR, S. 2004 Response of the wake of an isolated particle to an isotropic turbulent flow. *J. Fluid Mech.* **518**, 95–123.

BALACHANDAR, S. & EATON, J. K. 2010 Turbulent dispersed multiphase flow. *Annu. Rev. Fluid Mech.* **42**, 111–133.

BELLANI, G. 2011 Experimental studies of complex flows through image-based techniques. PhD thesis, Royal Institute of Technology, Stockholm.

BELLANI, G. & VARIANO, E. A. 2012 Slip-velocity and drag of large neutrally-buoyant particles in turbulent flows. *New J. Phys.* arXiv:1207.7142.

BENDAT, J. S. & PIERSOL, A. G. 2010 *Random Data: Analysis and Measurement Procedures*. John Wiley and Sons.

BENZI, R., ANGELIS, E. D., L'VOV, V. S. & PROCACCIA, I. 2005 Identification and calculation of the universal asymptote for drag reduction by polymers in wall bounded turbulence. *Phys. Rev. Lett.* **95**.

BURTON, T. M. & EATON, J. K. 2005 Fully resolved simulations of particle-turbulence interaction. *J. Fluid Mech.* **545**, 67–111.

CALZAVARINI, E., VOLK, R., LÉVÊQUE, E., PINTON, J. & TOSCHI, F. 2012 Impact of trailing wake drag on the statistical properties and dynamics of finite-sized particle in turbulence. *Physica* D **241**, 237–244.

CLAMEN, A. & GAUVIN, W. H. 1969 Effects of turbulence on the drag coefficients of spheres in a supercritical flow ŕegime. *AIChE J.* **15** (2), 184–189.

CLIFT, R., GRACE, J. R. & WEBER, M. E. 1978 *Bubbles, Drops, and Particles*. Academic.

EATON, J. K. 1991 Preferential concentration of particles by turbulence. *Phys. Fluids* A **3** (5), 1169–1178.

EATON, J. K. 2009 Two-way coupled turbulence simulations of gas-particle flows using point-particle tracking. *Intl J. Multiphase Flow* **35** (9), 792–800.

ELGHOBASHI, S. 1994 On predicting particle-laden turbulent flows. *Appl. Sci. Res.* **52**, 309–329.

ELGHOBASHI, S. 2003 On the physical mechanisms of two-way coupling in particle-laden isotropic turbulence. *Phys. Fluids* **15** (2), 315–329.

ELGHOBASHI, S. & TRUESDELL, G. C. 1993 On the two way interaction between homogeneous turbulence and dispersed solid particles. I. Turbulence modification. *Phys. Fluids* A **5**, 1790–1801.

EL KHOURY, G. K., ANDERSSON, H. I. & PETTERSEN, B. 2010 Crossflow past a prolate spheroid at Reynolds number of 10 000. *J. Fluid Mech.* **659**, 365–374.

FERRANTE, A. & ELGHOBASHI, S. 2004 On the physical mechanisms of drag reduction in a spatially developing turbulent boundary layer laden with microbubbles. *J. Fluid Mech.* **503**, 345–355.

GARCIA, M. H. 2008 *Sedimentation Engineering: Theories, Measurements, Modeling and Practice: Processes, Management, Modelling, and Practice*, 1st edn. American Society of Civil Engineers.

GEISS, S., DREIZLER, A., STOJANOVIC, Z. & CHRIGUI, M. 2004 Investigation of turbulence modification in a non-reactive two-phase flow. *Exp. Fluids* **36**, 344–354.

JEFFERY, G. B. 1922 The motion of ellipsoidal particles immersed in a viscous fluid. *Proc. R. Soc. Lond.* A 161–179.

JUMARS, P. A., TROWBRIDGE, J. H., BOSS, E. & KARP-BOSS, L. 2009 Turbulence-plankton interactions: a new cartoon. *Mar. Ecol.* **30** (2), 133–150.

KIM, I., ELGHOBASHI, S. & SIRIGNANO, W. A. 1998 On the equation for spherical-particle motion: effect of Reynolds and acceleration numbers. *J. Fluid Mech.* **367**, 221–253.

KOCH, D. L. & SHAQFEH, E. S. G. 1989 The instability of a dispersion of sedimenting spheroids. *J. Fluid Mech.* **209**, 521–542.

LIBERZON, A., GUALA, M., LÜTHI, B. & KINZELBACH, W. 2005 Turbulence in dilute polymer solutions. *Phys. Fluids* **17**, 031707.

LOTH, E. 2008 Drag of non-spherical solid particles of regular and irregular shape. *Powder Technol.* **182**, 342–353.

LUCCI, F., FERRANTE, A. & ELGHOBASHI, S. 2010 Modulation of isotropic turbulence by particles of Taylor length-scale size. *J. Fluid Mech.* **650**, 5–55.

LUCCI, F., FERRANTE, A. & ELGHOBASHI, S. 2011 Is stokes number an appropriate indicator for turbulence modulation by particles of Taylor-length-scale size? *Phys. Fluids* **23** (2), 025101.

LUNDELL, F. 2011 The effect of particle inertia on triaxial ellipsoids in creeping shear: from drift toward chaos to a single periodic solution. *Phys. Fluids* **23** (1), 011704.

LUNDELL, F., SÖDERBERG, L. D. & ALFREDSSON, P. H. 2010 Fluid mechanics of papermaking. *Annu. Rev. Fluid Mech.* **43**, 195–217.

MAXEY, M. R. & RILEY, J. J. 1983 Equation of motion for a small rigid sphere in a nonuniform flow. *Phys. Fluids* **26**, 883–890.

MORADIAN, N., TING, D. S.-K. & CHENG, S. 2009 The effects of freestream turbulence on the drag coefficient of a sphere. *Exp. Therm. Fluid Sci.* **33** (3), 460–471.

MORTENSEN, P. H., ANDERSSON, H. I., GILLISSEN, J. J. J. & BOERSMA, B. J. 2007 Particle spin in a turbulent shear flow. *Phys. Fluids* **19**, 078109.

MORTENSEN, P. H., ANDERSSON, H. I., GILLISSEN, J. J. J. & BOERSMA, B. J. 2008*a* Dynamics of prolate ellipsoidal particles in a turbulent channel flow. *Phys. Fluids* **20**, 0933202.

MORTENSEN, P. H., ANDERSSON, H. I., GILLISSEN, J. J. J. & BOERSMA, B. J. 2008*b* On the orientation of ellipsoidal particles in a turbulent shear flow. *Intl J. Multiphase Flow* **34**, 678–683.

OUELLETTE, N. T., O'MALLEY, P. J. J. & GOLLUB, J. P. 2008 Transport of finite-sized particles in chaotic flow. *Phys. Rev. Lett.* **101** (17), 174504.

POELMA, C., WESTERWEEL, J. & OOMS, G. 2006 Turbulence statistics from optical whole-field measurements in particle-laden turbulence. *Exp. Fluids* **40**, 347–363.

POELMA, C., WESTERWEEL, J. & OOMS, G. 2007 Particle–fluid interactions in grid-generated turbulence. *J. Fluid Mech.* **589**, 315–351.

POPE, S. B. 2000 *Turbulent Flows*. Cambridge University Press.

QURESHI, N. M., BOURGOIN, M., BAUDET, C., CARTELLIER, A. & GAGNE, Y. 2007 Turbulent transport of material particles: an experimental study of finite size effects. *Phys. Rev. Lett.* **99** (18), 184502–4.

SABBAN, L. & VAN HOUT, R. 2011 Measurements of pollen grain dispersal in still air and stationary, near homogeneous, isotropic turbulence. *J. Aerosol Sci.* **42** (12), 867–882.

SAW, E. W., SHAW, R. S., AYYALASOMAYAJULA, S., CHUANG, P. Y. & GYLFASON, A. 2008 Inertial clustering of particles in high-Reynolds-number turbulence. *Phys. Rev. Lett.* **100** (21), 214501–214505.

SCHRECK, S. & KLEIS, S. J. 1993 Modification of grid-generated turbulence by solid particles. *J. Fluid Mech.* **249**, 665–688.

SQUIRES, K. D. & EATON, J. K. 1990 Particle response and turbulence modification in isotropic turbulence. *Phys. Fluids* A **2**, 1191–1203.

TANAKA, T. & EATON, J. K. 2010 Sub-kolmogorov resolution partical image velocimetry measurements of particle-laden forced turbulence. *J. Fluid Mech.* **643**, 177–206.

TSINOBER, A. 2004 *An Informal Introduction to Turbulence*. Kluwer.

VARIANO, E. A. & COWEN, E. A. 2008 A random-jet-stirred turbulence tank. *J. Fluid Mech.* **604**, 1–32.

VIRK, P. S., MERRILL, E. W., MICKLEY, H. S. & SMITH, K. A. 1967 The toms phenomenon: turbulent pipe flow of dilute polymer solutions. *J. Fluid Mech.* **30**, 305–328.

XU, H. & BODENSCHATZ, E. 2008 Motion of inertial particles with size larger than kolmogorov scale in turbulent flows. *Physica* D **237** (14–17), 2095–2100.

YANG, T. S. & SHY, S. S. 2005 Two-way interaction between solid particles and homogeneous air turbulence: particle settling rate and turbulence modification measurements. *J. Fluid Mech.* **526**, 171–216.

YEO, K., DONG, S., CLIMENT, E. & MAXEY, M. R. 2010 Modulation of homogeneous turbulence seeded with finite size bubbles or particles. *Intl J. Multiphase Flow* **36** (3), 221–233.

ZASTAWNY, M., MALLOUPPAS, G., ZHAO, F. & VAN WACHEM, B. 2012 Derivation of drag and lift force and torque coefficients for non-spherical particles in flows. *Intl J. Multiphase Flow* **39**, 227–239.

ZHANG, H., AHMADI, G., FAN, F. G. & MCLAUGHLIN, J. B. 2001 Ellipsoidal particles transport and deposition in turbulent channel flows. *Intl J. Multiphase Flow* **27** (6), 971–1009.

ZHAO, L. & ANDERSSON, H. I. 2011 On particle spin in two-way coupled turbulent channel flow simulations. *Phys. Fluids* **23**, 093302.